Front. Phys. 13(4), 137105 (2018)
https://doi.org/10.1007/s11467-018-0796-9

RESEARCH ARTICLE

Tunable electronic structure and magnetic coupling in strained two-dimensional semiconductor $MnPSe_3$

Qi Pei[1], Xiao-Cha Wang[2], Ji-Jun Zou[3], Wen-Bo Mi[1,†]

[1] *Tianjin Key Laboratory of Low Dimensional Materials Physics and Preparation Technology, School of Science, Tianjin University, Tianjin 300354, China*
[2] *School of Electrical and Electronic Engineering, Tianjin University of Technology, Tianjin 300384, China*
[3] *Key Laboratory for Green Chemical Technology of the Ministry of Education, School of Chemical Engineering and Technology, Tianjin University, Tianjin 300354, China*
Corresponding author. E-mail: †miwenbo@tju.edu.cn
Received February 11, 2018; accepted April 24, 2018

The electronic structures and magnetic properties of strained monolayer $MnPSe_3$ are investigated systematically via first-principles calculations. It is found that the magnetic ground state of monolayer $MnPSe_3$ can be significantly affected by biaxial strain engineering, while the semiconducting characteristics are well-preserved. Owing to the sensitivity of the magnetic coupling towards structural deformation, a biaxial tensile strain of approximately 13% can lead to an antiferromagnetic (AFM)-ferromagnetic (FM) transition. The strain-dependent magnetic stability is mainly attributed to the competition of the direct AFM interaction and indirect FM superexchange interaction between the two nearest-neighbor Mn atoms. In addition, we find that FM $MnPSe_3$ is an intrinsic half semiconductor with large spin exchange splitting in the conduction bands, which is crucial for the spin-polarized carrier injection and detection. The sensitive interdependence among the external stimuli, electronic structure, and magnetic coupling makes monolayer $MnPSe_3$ a promising candidate for spintronics.

Keywords two-dimensional semiconductor, $MnPSe_3$, strain engineering, electronic structure, magnetic coupling

PACS numbers 71.15.Mb, 73.22.-f, 75.50.Pp, 75.30.Et

1 Introduction

Recently, the emergence of two-dimensional (2D) materials has attracted widespread interest [1–4]. In particular, 2D magnetic semiconductors, which possess both semiconducting and magnetic characteristics, have been considered as promising candidates for low-dimensional spintronic devices. In general, magnetic semiconductors can be classified into two categories: intrinsic magnetic semiconductors and diluted magnetic semiconductors. Compared with intrinsic magnetic semiconductor, the diluted magnetic semiconductor can be easily obtained by doping the nonmagnetic semiconductor with transition metals [5–7]. However, there are problems in the synthesis of diluted magnetic semiconductors, such as the low solubility and rich boundary defects. Therefore, finding experimentally feasible methods for the fabrication of magnetic semiconductors is critical. At present, the strategy of exfoliating single layers from bulk layered structures has been comprehensively investigated. Following this approach, recent theoretical studies have proposed potential magnetic 2D van der Waals (vdW) materials, including transition-metal carbides and nitride MXenes [8], Cr-based ternary tritellurides $CrXTe_3$ (X = Si, Ge) [9–11], V-based dichalcogenides VX_2 (X = S, Se) [12], trihalides CrX_3 (X = F, Cl, Br, I) [13], and transition-metal P trichalcogenides MPX_3 (M = Fe, Mn, Ni; X = S, Se) [14–16]. As a representative of the MPX_3 family, monolayer $MnPSe_3$ exhibits particular advantages in solar energy-related applications and novel spin-valley coupling physics [17, 18], endowing this 2D crystal with great potential in spintronics.

The control of the spin ordering is another key issue for the application of spintronic devices. The spin ordering of magnetic materials should be deliberately modulated

*arXiv: 1804.10399.

by external stimuli, such as the electric field, atomic vacancy, adsorption, doping, or elastic strain engineering [19–22]. Among these external factors, mechanical strain is commonly regarded as an effective route to induce the change of the crystal structure, the modification of the orbital overlap, and the emergence of charge distribution. The excellent mechanical flexibility of 2D magnets provides further proof of the feasibility of strain engineering [23, 24]. Many theoretical reports have indicated the tunable electronic structures and magnetic characteristics in stained monolayers [12, 25–28]. Experimentally, a remarkable advance in applying tunable biaxial strain to 2D materials was proposed by Ding *et al.* [29]. Using a thin layer of polymethylmethacrylate as glue, single-layer graphene can be transferred onto a SiO_2-covered piezoelectric substrate. Then, applying a bias voltage to the piezoelectric substrate results in an out-of-plane electric field, leading to an in-plane strain. This technique not only makes it possible to study the strain-related behaviors of low-dimensional materials but also inspires new ideas and methods for strain application.

In this study, the electronic and magnetic properties of monolayer $MnPSe_3$, as well as the intercoupling between the strain and magnetism, are systematically investigated using density functional theory (DFT). It is found that pristine monolayer $MnPSe_3$ is an intrinsic semiconductor with antiferromagnetic (AFM) ordering. The stability of AFM coupling can be significantly weakened by applying elastic biaxial strains. An AFM-ferromagnetic (FM) transition occurs under a large tensile strain beyond 13%. The physical mechanism of such a phenomenon is further studied, and a strain-related competition between the direct exchange interaction and the indirect superexchange interaction is proposed. In addition, monolayer $MnPSe_3$ with FM coupling exhibits robust semiconducting characteristics, with fully spin-polarized valence and conduction band edges. These novel properties render monolayer $MnPSe_3$ a promising platform for exploring magnetic phenomena and offer a promising avenue for fabricating controllable and tunable spintronic devices.

2 Computational details

Our calculations are performed in the framework of DFT, using a plane-wave basis [30] set as implemented in the VASP code [31]. The generalized gradient approximation (GGA) parameterized by Perdew–Burke–Ernzerhof [32] is utilized to describe the exchange-correlation functional. Because the GGA cannot properly describe strongly correlated systems with partially filled d subshells, we use Hubbard U terms (5 eV for Mn) to describe the on-site electron–electron Coulomb repulsion, as suggested in the literature [33]. The vdW-D2 correction [34] is used together with GGA+U to add the longer-ranged correlation in evaluating the vdW interaction between the monolayers. Kohn–Sham single-particle wavefunctions are expanded in the plane wave basis set with a kinetic energy truncation at 500 eV. The Monkhorst–Pack scheme is adopted for k-point sampling employing a $7 \times 7 \times 1$ Γ-centered grid. The energy and force convergence criteria on each atom are less than 10^{-6} eV and 0.01 eV/Å, respectively. A $2 \times 2 \times 1$ supercell model including eight Mn atoms is adopted in the calculation to identify the preferred magnetic ground state (GS), and a 20 Å vacuum slab is inserted perpendicularly on the top of the $MnPSe_3$ surface to minimize the interaction between periodic images.

3 Results and discussion

Bulk $MnPSe_3$ has been proposed to be an AFM semiconductor with an optical energy gap of 2.27 eV [35] and a Neél temperature of 74 K [36]. Because a relatively weak vdW force holds together the layered compound, monolayer $MnPSe_3$ is easily exploited from its corresponding bulk phase. As shown in Figs. 1(a) and (b), each $MnPSe_3$ unit cell is composited of two Mn^{2+} ions and one $[P_2Se_6]^{4-}$ cluster. A Mn atom is located at the center of a distorted octahedron with six Se atoms arranged in a trigonal antiprism structure. The dumbbell-like P dimer in the $[P_2Se_6]^{4-}$ bipyramid constrains six neighboring Se atoms to form two Se trimers with a relative in-plane twist of 60°, perpendicular to the honeycomb plane. The formal valences of the Mn, P, and Se atoms are +2, +4, and −2, respectively. According to Hund's rule, Mn^{2+} with a $3d^5$ electronic configuration exhibits a high spin state.

The lattice structure of the $MnPSe_3$ monolayer is optimized to observe the resulting lattice parameters. After full relaxation, the lattice constant of the FM structure (6.409 Å) is similar to that of the AFM structure (6.403 Å), suggesting that there is no correlation between the lattice parameter and the magnetic structure. The agreement of the optimized lattice constant with the experimental value (6.387 Å) [36] also reveals that GGA+U can correctly describe the structural and electronic properties of monolayer $MnPSe_3$, verifying the rationality of our parameters in the calculation. The spin density for the FM and AFM configurations are calculated using the equation $\rho = \rho_\uparrow - \rho_\downarrow$, where $\rho_\uparrow$ and $\rho_\downarrow$ represent the spin-up and spin-down charge densities, respectively. As illustrated in Fig. 1(c), the major magnetism in monolayer $MnPSe_3$ with FM ordering is due to Mn atoms. The local magnetic moment of a Mn atom is textured to be approximately 4.613 μ_B, and each P and Se atom

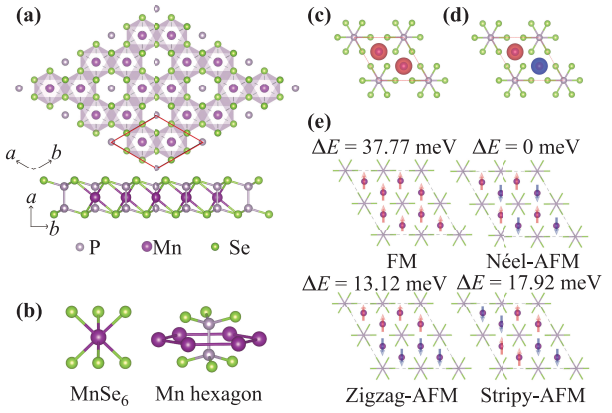

Fig. 1 **(a)** Top and side views of monolayer $MnPSe_3$. The unit cell is indicated by red solid line. The grey, purple and green spheres represent the P, Mn, and Se atoms, respectively. **(b)** Atomic structures of a distorted $MnSe_6$ octahedron and $[P_2Se_6]^{4-}$ bipyramids enclosed with hexagonal Mn atoms. Isosurface plots of the spin charge density for **(c)** FM and **(d)** AFM configurations. The isosurface value is set up to ± 0.1 e/Å^3. The blue and red isosurfaces represent spin-up and spin-down charge densities, respectively. **(e)** Four possible spin configurations and their relative energy ΔE (meV/unitcell) with respect to the Néel-AFM configuration.

carries a magnetic moment of approximately 0.016 and 0.023 μ_B, respectively. Similarly, the spin density for the AFM configuration in Fig. 1(d) is primarily due to two Mn atoms with opposite spin magnetic moments (4.598 μ_B), while the magnetic moments of P and Se can be neglected. The total magnetic moment of the AFM form is exactly 0 μ_B for the intrinsic AFM coupling of Mn^{2+} ions.

To confirm the most preferable magnetic coupling between the Mn atoms, with the exception of the FM and regular AFM (Néel) orders, we consider two additional AFM configurations: zigzag-AFM and stripy-AFM, as shown in Fig. 1(e). After they are differentiated energetically, the relative energy differences ΔE (absolute value) with respect to the Néel-AFM configuration are 0, 37.77, 13.12, and 17.92 meV for Néel-AFM, FM, zigzag-AFM, and stripy-AFM, respectively. Our calculations clearly show that the Néel-AFM order has the minimum energy, indicating that the GS is of Néel order. Unless otherwise indicated, AFM order refers to the AFM-Néel order hereinafter. Additionally, the non-magnetic (NM) state can be neglected owing to the great energy disparity between the NM state and magnetic states.

To evaluate the effect of strain engineering on the electronic and magnetic properties, a series of *xy*-plane biaxial strains are applied to monolayer $MnPSe_3$. As shown in Fig. 2(c), we stretch or shrunk the lattice constants uniformly to simulate the tensile and compressive strains. The strain can be estimated by considering the lattice constants quantitatively as $\varepsilon = (a - a_0)/a_0$, where a_0 and a are the lattice constants of the original and strained models, respectively. A distinction between tensile and compressive strains is made by defining $\varepsilon > 0$ or $\varepsilon < 0$. The variation of the energy difference between the AFM and FM coupling in the biaxially strained systems is depicted in Fig. 2(a). When the tensile strain changes from 0% to 5%, the energy difference $\Delta E_{AFM\text{-}FM}$ increases from -37.77 to -20.30 meV per formula unit, suggesting that the AFM state is significantly weakened and tends towards instability. When the tensile strain continues to increase, a clear magnetic phase transition from AFM to FM is achieved in the presence of a relatively large strain of approximately 13%. Moreover, the FM stability can be further enhanced under a 15% tensile strain. Because large strain modulations (beyond 10%) have already been observed in many ultrathin 2D systems, such as graphene [37] and MoS_2 [25] employing either the three-point bending configuration or piezoelectric substrates, we are confident that a 13% tensile strain can also be realized in monolayer $MnPSe_3$. Hence, strain engineering can be considered as a potential modulating artifice to realize the transition of the magnetic phase in monolayer $MnPSe_3$. Meanwhile, the distance between the two nearest-neighbor (NN) Mn atoms increases linearly from 3.515 to 4.267 Å as the biaxial strain changes from -5% to 15%. We calculate the total energies for all possible magnetic configurations under each biaxial strain, and the variation of the energy difference ($\Delta E_{AFM\text{-}zigzag}$ and $\Delta E_{AFM\text{-}stripy}$) is shown in Fig. S1 of the Supplementary Information. As no other magnetic phase transition occurs within the biaxial strain range that we consider, we focus on the AFM-FM transition.

Figure 2(b) shows the variation of the bandgap in the biaxially strained systems. In the strain region of -5% to 3%, the bandgap increases gradually. However, when the tensile strain increases continuously, the bandgap values begin to decrease. A sharp bandgap decrease from 1.09 to 0.67 eV occurs at the tensile strain of 13%, corresponding to the magnetic phase transition from AFM to FM. In addition, the robustness of the semiconducting property against a wide range of biaxial strain intensities should be noted.

The band structure (BS) and density of states (DOS) within the energy window of -3 to 3 eV are calculated to reveal the electronic properties of strained monolayer $MnPSe_3$. Figures 3(a)–(f) correspond to the system under strains of -5%, 0%, 5%, 10%, 13%, and 15%, respectively. For the pristine monolayer [see Fig. 3(b)], $MnPSe_3$ is a semiconductor with a direct bandgap of 1.83 eV, in accordance with previous theoretical results [14, 17]. The valence bands (VB) near Fermi level mainly consist of Se and Mn atoms, whereas the conduction bands (CBs) comprise Se, Mn, and P atoms. A comparison of

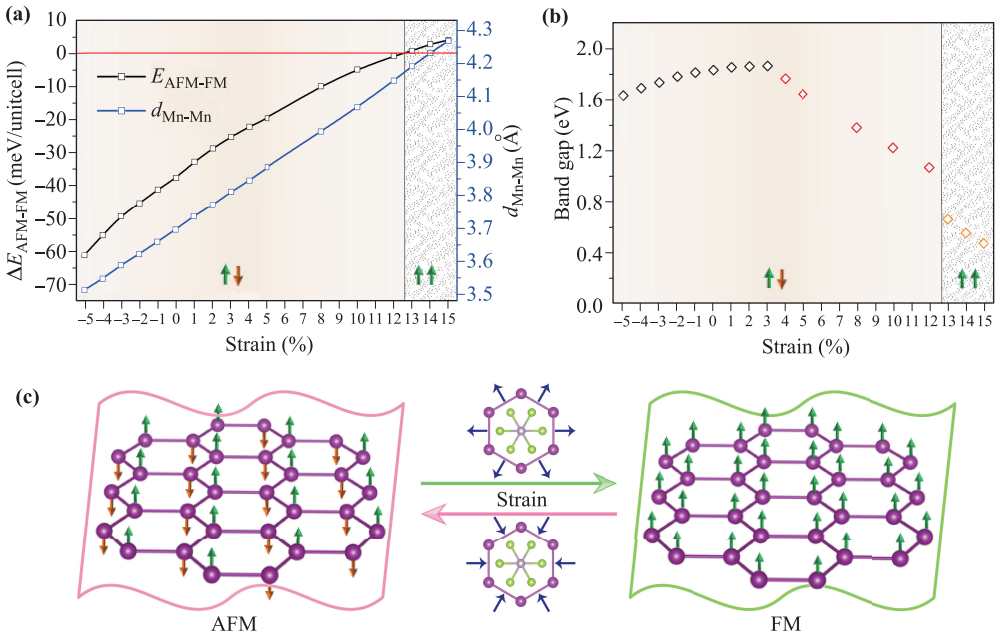

Fig. 2 **(a)** Variation of the energy difference between the AFM and FM coupling and the nearest Mn-Mn distance in biaxial strained systems. Negative value indicates that the FM configuration is less stable than the AFM configuration. **(b)** Variation of the band gap at different biaxial strains. **(c)** Schematic plot of the effect of biaxial strain on the magnetic coupling.

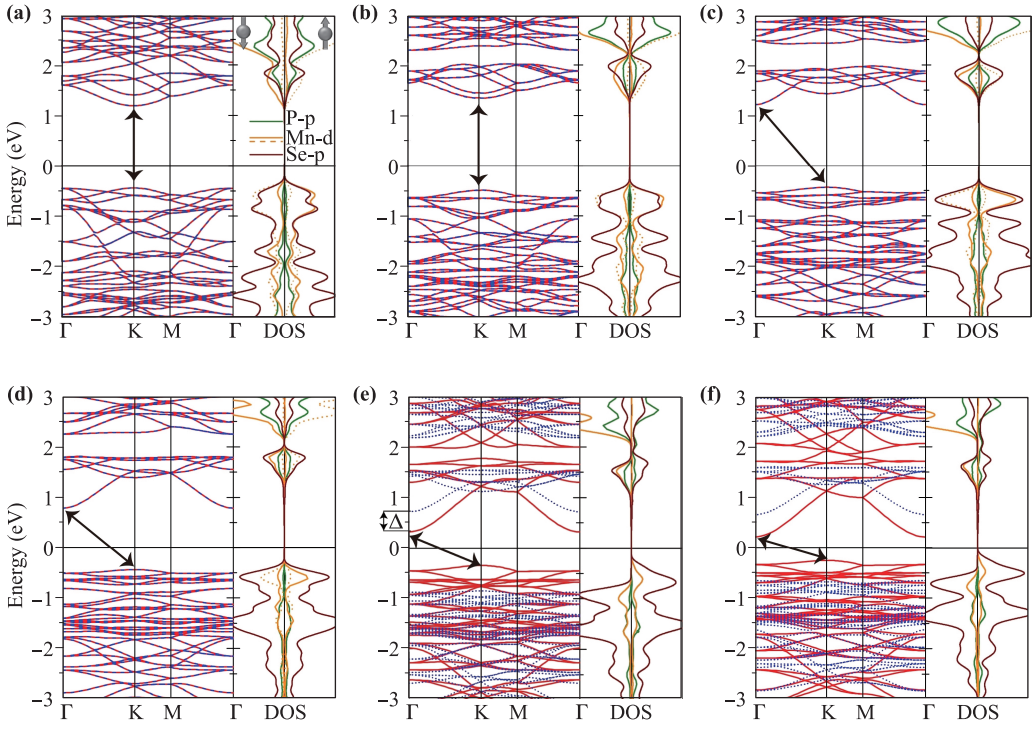

Fig. 3 Band structures and density of states for monolayer $MnPSe_3$ at the biaxial strain of **(a)** −5%, **(b)** 0%, **(c)** 5%, **(d)** 10%, **(e)** 13% and **(f)** 15%. Fermi level is indicated by the vertical solid line and set to zero.

Figs. 3(c) and (e) reveals that as the lattice constants increase, the contribution of the Se p orbitals to the states in the valence-band maximum (VBM) range up to −0.5 eV increases. The peak of the Se projected DOS (PDOS)

in this energy range shifts to higher energies. Moreover, by applying a 5% tensile strain, BS calculations reveal an indirect semiconductor with a conduction-band minimum and VBM at the points Γ and K, respectively. The band transition from direct to indirect also makes the gap decrease to 1.64 eV, which is well-consistent with the variation tendency shown in Fig. 2(b). When the strain increases to 13%, the FM state is more stable than the AFM state. The occupied states near the Fermi level have a major contribution from Se atoms, while the unoccupied states in the vicinity of the Fermi level are derived from Se, Mn, and P atoms. Examination of the PDOS of Mn and Se atoms shows that the Mn d states are relatively delocalized and hybridized with the Se p states, indicating that the indirect p–d exchange interaction plays an important role in the FM coupling. In addition, FM $MnPSe_3$ is an indirect semiconductor with a bandgap of 0.66 eV. The bands in the spin-up and spin-down channels do not overlap, suggesting intrinsic ferromagnetism. In particular, the VB and CB edges of FM $MnPSe_3$ are fully spin-polarized in the same spin direction, indicating that the FM $MnPSe_3$ is a half semiconductor. A large spin exchange splitting of 0.40 eV [labeled as Δ in Fig. 3(e)] in the CB is observed, which is not only essential for the spin-polarized carrier injection and detection [10] but also crucial for gaining the half-metallic property by shifting the relative position of the Fermi level. The exchange splitting can be further increased to 0.44 eV at a tensile strain of 15%.

Because our calculations show that the magnetic moments are concentrated on the metal atom sites [see Figs. 1(c) and (d)], we characterize the magnetic properties of $MnPSe_3$ using an effective Heisenberg model Hamiltonian on a honeycomb lattice:

$$H = \sum_{\langle ij \rangle} J_1 \boldsymbol{S}_i \cdot \boldsymbol{S}_j + \sum_{\langle ij \rangle} J_2 \boldsymbol{S}_i \cdot \boldsymbol{S}_j + \sum_{\langle ij \rangle} J_3 \boldsymbol{S}_i \cdot \boldsymbol{S}_j, \quad (1)$$

where $J_{1,2,3}$ represents the exchange interactions between the NN, second NN, and third NN spins. $\boldsymbol{S}_i$ represents the total spin magnetic moment of the atomic site i. To extract the magnetic exchange interactions, the lattice is fixed to that of the most energetically favorable spin confirmation, and the energies for different spin configurations are computed. Using Equation (1), the magnetic energy can be explicitly expressed as

$$E_{\mathrm{FM/Néel}} = E_0 + (\pm 3J_1 + 6J_2 \pm 3J_3)|S|^2, \quad (2)$$

$$E_{\mathrm{zigzag/stripy}} = E_0 + (\pm J_1 - 2J_2 \mp 3J_3)|S|^2. \quad (3)$$

We then obtain the lattice constant, GS, and exchange coupling constants for pristine and biaxially strained $MnPSe_3$. As listed in Table S1, the NN interaction J_1, the second NN interaction J_2 and the third NN interaction J_3 are all AFM. J_2 (0.02 meV) is one order of magnitude smaller than J_1 (0.195 meV) and significantly smaller than J_3 (0.103 meV). These findings are consistent with previous studies on $MnPS_3$ and $MnPSe_3$ [16, 38, 39]. More importantly, the J_2 and J_3 interactions in transition-metal trichalcogenide monolayers are always AFM [40].

To understand the microscopic origin of the exchange interactions in monolayer $MnPSe_3$, the possible electron-hopping paths for J_1, J_2, and J_3 interactions are plotted. As shown in Fig. 4(a), electrons hopping for a J_1 interaction mainly follow two paths. One is the short-range direct interaction between two neighboring Mn ions (Mn-Mn), which is robustly AFM for the half-filled high-spin d^5 state of Mn, and the other is the more long-range Mn-Se-Mn superexchange interaction with an angle of 84.1°. According to the well-known Goodenough–Kanamori–Anderson (GKA) rules [41, 42], systems with cation–anion–cation bond angles of 90° prefer weak FM ordering, and 180° superexchange interactions are AFM. Therefore, the Mn-Se-Mn angle (84.1° close to 90°) in superexchange is FM. Owing to the closed d shell on Mn ions and the large electron excitation energy from the Se p orbital to the Mn d orbital, the direct AFM exchange interaction dominates over the FM superexchange interaction. Consequently, J_1 is expected to be AFM.

In Figs. 4(b) and (c), there are several hopping paths for J_2 and J_3, where the cations are separated by two anions. According to the geometry, the most probable paths should involve two Se anions on the same plane with the shortest Se–Se distance. For this reason, J_2 and J_3 can be regarded as super-superexchange interactions. Because the rules for the cation–anion–anion–cation path are similar to those for cation–anion–cation

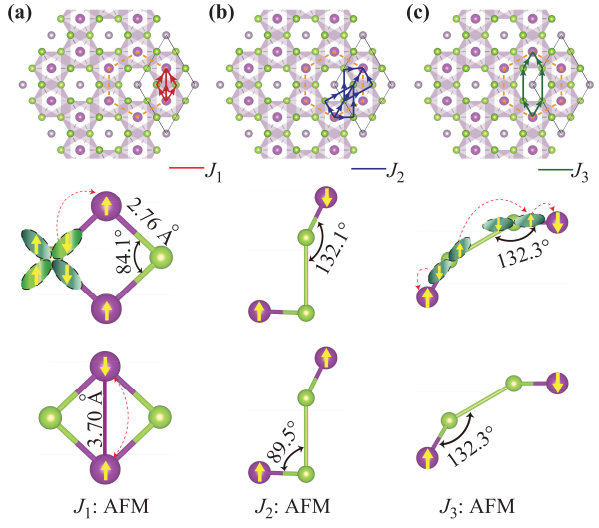

Fig. 4 Schematic diagram of possible paths for the **(a)** NN, **(b)** second NN and **(c)** third NN magnetic exchange interactions in monolayer $MnPSe_3$.

interactions, 180° and 90° are also two criterion angles for AFM and FM interactions, respectively. However, for interactions with intermediate angles between 90° and 180°, a crossover angle of 127 ± 0.6° is related to the AFM-FM transition [43]. Zhang *et al.* [44] proposed that a cation–anion–anion angle larger than 130° leads to AFM interaction, while an angle of approximately 90° contributes to an FM interaction. According to the aforementioned findings, the most possible electron-hopping path for J_3 contains two cation–anion–anion angles, which are both 132.3°, resulting in strong AFM contributions. Regarding the J_2 interaction, although the two cation–anion–anion angles of 132.1° and 89.5° contribute to AFM and FM interactions, respectively, the resulting extended J_2 exhibits the AFM characteristic owing to the AFM dominance in monolayer $MnPSe_3$ [44]. Compared with J_1 and J_3, J_2 is relatively weak for involving small Se-Se hybridizations. Hence, we suppose that the AFM-FM transition mainly depends on the significant competition between the AFM exchange interaction and FM superexchange interaction from the NN interaction J_1. With the increase of the biaxial strain, the cation–anion–anion angles always change within the criterion angle range. J_2 and J_3 are expected to decrease in magnitude because of the increasing atomic distances, while the variation of J_1 is subtler. A rapid reduction of the direct exchange interaction and a relatively slow reduction of the indirect superexchange interaction give rise to the impairment of the AFM stability and the resultant enhancement of the FM stability. Once the tensile strain is sufficiently large, magnetic phase reversal can be realized by changing the signs (positive and negative) of the energy difference between AFM and FM; thus, the AFM-FM transition can be well-explained.

Additionally, the uniaxial strain effect on the magnetic phase transition was recognized in a previous $CrPS_4$ monolayer [45]. In this work, the uniaxial strain engineering is further tested. The results are listed in Table S2 of the Supplementary Information. Generally, both the uniform biaxial and uniaxial strains can trigger the modification of the total energies, resulting in the magnetic phase transition. However, the effect is weaker for uniaxial strain in monolayer $MnPSe_3$. A relatively large uniaxial strain is required to alter the AFM-FM transition.

4 Conclusion

The electronic structures and magnetic properties of strained monolayer $MnPSe_3$ are systematically surveyed. Our *ab initio* calculations show that the 2D $MnPSe_3$ is an AFM semiconductor. In particular, the AFM stability can be substantially influenced by strain engineering, and an AFM to FM transition occurs under a large tensile strain, indicating that the strain can be used effectively for modulating the magnetic phase. The underlying physical mechanism of the strain-dependent magnetic stability is further elucidated as the competition of the direct exchange and indirect superexchange interactions between the two NN Mn atoms. Our results provide strong evidence that strain can be an effective pathway to induce or modulate the magnetic properties of 2D crystals and introduce $MnPSe_3$ as a promising 2D magnet.

Electronic supplementary material Supplementary material is available in the online version of this article at https://doi.org/10.1007/s11467-018-0796-9 and is accessible for authorized users.

Acknowledgements This work was supported by the National Natural Science Foundation of China (Grant Nos. 51671142, U1632152, and 51661145026) and the Key Project of Natural Science Foundation of Tianjin City (Grant No. 16JCZDJC37300).

References

1. K. S. Novoselov, A. K. Geim, S. V. Morozov, D. Jiang, Y. Zhang, S. V. Dubonos, I. V. Grigorieva, and A. A. Firsov, Electric field effect in atomically thin carbon films, *Science* 306(5696), 666 (2004)
2. K. S. Novoselov, A. K. Geim, S. V. Morozov, D. Jiang, M. I. Katsnelson, I. V. Grigorieva, S. V. Dubonos, and A. A. Firsov, Two-dimensional gas of massless Dirac fermions in graphene, *Nature* 438(7065), 197 (2005)
3. Y. Zhang, Y. W. Tan, H. L. Stormer, and P. Kim, Experimental observation of the quantum Hall effect and Berry's phase in graphene, *Nature* 438(7065), 201 (2005)
4. A. K. Geim and K. S. Novoselov, The rise of graphene, *Nat. Mater.* 6(3), 183 (2007)
5. F. Banhart, J. Kotakoski, and A. V. Krasheninnikov, Structural defects in graphene, *ACS Nano* 5(1), 26 (2011)
6. H. Pan, J. B. Yi, L. Shen, R. Q. Wu, J. H. Yang, J. Y. Lin, Y. P. Feng, J. Ding, L. H. Van, and J. H. Yin, Room-temperature ferromagnetism in carbon-doped ZnO, *Phys. Rev. Lett.* 99(12), 127201 (2007)
7. C. Cao, M. Wu, J. Jiang, and H. P. Cheng, Transition metal adatom and dimer adsorbed on graphene: Induced magnetization and electronic structures, *Phys. Rev. B* 81(20), 205424 (2010)
8. M. Naguib, V. N. Mochalin, M. W. Barsoum, and Y. Gogotsi, MXenes: A new family of two-dimensional materials, *Adv. Mater.* 26(7), 992 (2014)
9. S. Lebègue, T. Björkman, M. Klintenberg, R. M. Nieminen, and O. Eriksson, Two-dimensional materials from data filtering and *ab initio* calculations, *Phys. Rev. X* 3(3), 031002 (2013)

10. X. Li and J. Yang, CrXTe$_3$ (X=Si, Ge) nanosheets: Two dimensional intrinsic ferromagnetic semiconductors, *J. Mater. Chem. C Mater. Opt. Electron. Devices* 2(34), 7071 (2014)
11. M. W. Lin, H. L. Zhuang, J. Yan, T. Z. Ward, A. A. Puretzky, C. M. Rouleau, Z. Gai, L. Liang, V. Meunier, B. G. Sumpter, P. Ganesh, P. R. C. Kent, D. B. Geohegan, D. G. Mandrus, and K. Xiao, Ultrathin nanosheets of CrSiTe$_3$: A semiconducting two-dimensional ferromagnetic material, *J. Mater. Chem. C* 4(2), 315 (2016)
12. Y. Ma, Y. Dai, M. Guo, C. Niu, Y. Zhu, and B. Huang, Evidence of the existence of magnetism in pristine VX_2 monolayers (X = S, Se) and their strain-induced tunable magnetic properties, *ACS Nano* 6(2), 1695 (2012)
13. W. B. Zhang, Q. Qu, P. Zhu, and C. H. Lam, Robust intrinsic ferromagnetism and half semiconductivity in stable two-dimensional single-layer chromium trihalides, *J. Mater. Chem. C* 3(48), 12457 (2015)
14. X. X. Li, X. J. Wu, and J. L. Yang, Half-metallicity in MnPSe$_3$ exfoliated nanosheet with carrier doping, *J. Am. Chem. Soc.* 136(31), 11065 (2014)
15. X. Zhang, X. Zhao, D. Wu, Y. Jing, and Z. Zhou, MnPSe$_3$ monolayer: a promising 2D visible-light photohydrolytic catalyst with high carrier mobility, *Adv. Sci.* 3(10), 1600062 (2016)
16. B. L. Chittari, Y. Park, D. Lee, M. Han, A. H. MacDonald, E. Hwang, and J. Jung, Electronic and magnetic properties of single-layer MPX_3 metal phosphorous trichalcogenides, *Phys. Rev. B* 94(18), 184428 (2016)
17. X. Li, T. Cao, Q. Niu, J. Shi, and J. Feng, Coupling the valley degree of freedom to antiferromagnetic order, *Proc. Natl. Acad. Sci. USA* 110(10), 3738 (2013)
18. Q. Pei, Y. Song, X. Wang, J. Zou, and W. Mi, Superior electronic structure in two-dimensional MnPSe$_3$/MoS$_2$ van der Waals heterostructures, *Sci. Rep.* 7(1), 9504 (2017)
19. K. F. Mak, C. H. Lui, J. Shan, and T. F. Heinz, Observation of an electric-field-induced band gap in bilayer graphene by infrared spectroscopy, *Phys. Rev. Lett.* 102(25), 256405 (2009)
20. Y. Zhou, Z. Wang, P. Yang, X. Zu, L. Yang, X. Sun, and F. Gao, Tensile strain switched ferromagnetism in layered NbS$_2$ and NbSe$_2$, *ACS Nano* 6(11), 9727 (2012)
21. Y. C. Cheng, Q. Y. Zhang, and U. Schwingenschlögl, Valley polarization in magnetically doped single-layer transition-metal dichalcogenides, *Phys. Rev. B* 89(15), 155429 (2014)
22. K. Sawada, F. Ishii, M. Saito, S. Okada, and T. Kawai, Phase control of graphene nanoribbon by carrier doping: Appearance of noncollinear magnetism, *Nano Lett.* 9(1), 269 (2009)
23. F. Li and Z. Chen, Tuning electronic and magnetic properties of MoO$_3$ sheets by cutting, hydrogenation, and external strain: A computational investigation, *Nanoscale* 5(12), 5321 (2013)
24. H. H. Pérez-Garza, E. W. Kievit, G. F. Schneider, and U. Staufer, Highly strained graphene samples of varying thickness and comparison of their behavior, *Nanotechnology* 25(46), 465708 (2014)
25. S. Bertolazzi, J. Brivio, and A. Kis, Stretching and breaking of ultrathin MoS$_2$, *ACS Nano* 5(12), 9703 (2011)
26. X. Chen, J. Qi, and D. Shi, Strain-engineering of magnetic coupling in two-dimensional magnetic semiconductor CrSiTe$_3$: competition of direct exchange interaction and superexchange interaction, *Phys. Lett. A* 379(1–2), 60 (2015)
27. Y. Ma, Y. Dai, M. Guo, C. Niu, L. Yu, and B. Huang, Strain-induced magnetic transitions in half-fluorinated single layers of BN, GaN and graphene, *Nanoscale* 3(5), 2301 (2011)
28. L. Kou, C. Tang, W. Guo, and C. Chen, Tunable magnetism in strained graphene with topological line defect, *ACS Nano* 5(2), 1012 (2011)
29. F. Ding, H. Ji, Y. Chen, A. Herklotz, K. Dörr, Y. Mei, A. Rastelli, and O. G. Schmidt, Stretchable graphene: A close look at fundamental parameters through biaxial straining, *Nano Lett.* 10(9), 3453 (2010)
30. G. Kresse and J. Furthmüller, Efficient iterative schemes for *ab initio* total-energy calculations using a plane-wave basis set, *Phys. Rev. B* 54(16), 11169 (1996)
31. G. Kresse and J. Furthmüller, Efficiency of *ab-initio* total energy calculations for metals and semiconductors using a plane-wave basis set, *Comput. Mater. Sci.* 6(1), 15 (1996)
32. J. P. Perdew, K. Burke, and M. Ernzerhof, Generalized gradient approximation made simple, *Phys. Rev. Lett.* 77(18), 3865 (1996)
33. S. L. Dudarev, G. A. Botton, S. Y. Savrasov, C. J. Humphreys, and A. P. Sutton, Electron-energy-loss spectra and the structural stability of nickel oxide: An LSDA+U study, *Phys. Rev. B* 57(3), 1505 (1998)
34. S. Grimme, Semiempirical GGA-type density functional constructed with a long-range dispersion correction, *J. Comput. Chem.* 27(15), 1787 (2006)
35. V. Grasso and L. Silipigni, Optical absorption and reflectivity study of the layered MnPSe$_3$ seleniophosphate, *J. Opt. Soc. Am. B* 16(1), 132 (1999)
36. A. Wiedenmann, J. Rossat-Mignod, A. Louisy, R. Brec, and J. Rouxel, Neutron diffraction study of the layered compounds MnPSe$_3$ and FePSe$_3$, *Solid State Commun.* 40(12), 1067 (1981)
37. T. Zhu and J. Li, Ultra-strength materials, *Prog. Mater. Sci.* 55(7), 710 (2010)
38. A. R. Wildes, B. Roessli, B. Lebech, and K. W. Godfrey, Spin waves and the critical behaviour of the magnetization in., *J. Phys.: Condens. Matter* 10(28), 6417 (1998)
39. K. Okuda, K. Kurosawa, S. Saito, M. Honda, Z. Yu, and M. Date, Magnetic properties of layered compound MnPS$_3$, *J. Phys. Soc. Jpn.* 55(12), 4456 (1986)

40. N. Sivadas, M. W. Daniels, R. H. Swendsen, S. Okamoto, and D. Xiao, Magnetic ground state of semiconducting transition-metal trichalcogenide monolayers, *Phys. Rev. B* 91(23), 235425 (2015)

41. J. B. Goodenough, Theory of the role of covalence in the perovskite-type manganites [La, M(II)]MnO_3, *Phys. Rev.* 100(2), 564 (1955)

42. J. Kanamori, Crystal distortion in magnetic compounds, *J. Appl. Phys.* 31(5), S14 (1960)

43. M. A. Subramanian, A. P. Ramirez, and W. J. Marshall, Structural tuning of ferromagnetism in a 3D cuprate perovskite, *Phys. Rev. Lett.* 82(7), 1558 (1999)

44. W. B. Zhang, Q. Qu, P. Zhu, and C. H. Lam, Robust intrinsic ferromagnetism and half semiconductivity in stable two-dimensional single-layer chromium trihalides, *J. Mater. Chem. C* 3(48), 12457 (2015)

45. M. Joe, H. Lee, M. M. Alyörük, J. Lee, S. Y. Kim, C. Lee, and J. H. Lee, A comprehensive study of piezomagnetic response in $CrPS_4$ monolayer: Mechanical, electronic properties and magnetic ordering under strains, *J. Phys.: Condens. Matter* 29(40), 405801 (2017)